ACS NANO

ARTICLE

Phase Restructuring in Transition Metal Dichalcogenides for Highly Stable Energy Storage

Kai Leng,[†,§] Zhongxin Chen,[†] Xiaoxu Zhao,[†] Wei Tang,[†] Bingbing Tian,[†] Chang Tai Nai,[†] Wu Zhou,[∥] and Kian Ping Loh*[,†,‡]

[†]Department of Chemistry, National University of Singapore, 3 Science Drive 3, Singapore 117543
[‡]Center for Advanced 2D Materials and Graphene Research Centre, 2 Science Drive 2, Singapore 117526
[§]Solar Energy Research Institute of Singapore (SERIS), 7 Engineering Drive 1, Singapore 117574
[∥]Materials Science and Technology Division, Oak Ridge National Laboratory, Oak Ridge, Tennessee 37831, United States

Ⓢ Supporting Information

ABSTRACT: Achieving homogeneous phase transition and uniform charge distribution is essential for good cycle stability and high capacity when phase conversion materials are used as electrodes. Herein, we show that chemical lithiation of bulk $2H\text{-}MoS_2$ distorts its crystalline domains in three primary directions to produce mosaic-like $1T'$ nanocrystalline domains, which improve phase and charge uniformity during subsequent electrochemical phase conversion. $1T'\text{-}Li_xMoS_2$, a macroscopic dense material with interconnected nanoscale grains, shows excellent cycle stability and rate capability in a lithium rechargeable battery compared to bulk or exfoliated-restacked MoS_2. Transmission electron microscopy studies reveal that the interconnected MoS_2 nanocrystals created during the phase change process are reformable even after multiple cycles of galvanostatic charging/discharging, which allows them to play important roles in the long term cycling performance of the chemically intercalated TMD materials. These studies shed light on how bulk TMDs can be processed into quasi-2D nanophase material for stable energy storage.

KEYWORDS: 2D materials, lithium ion batteries, phase engineering, energy storage, transition metal dichalcogenides
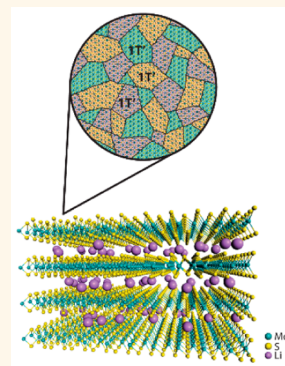
Transition metal dichalcogenides (TMDs) can exist in different polymorphs depending on the electron population in the d orbitals, which can be modified by charge transfer from intercalants such as lithium and sodium ions. Polymorph engineering of MoS_2 and the structure–property correlation arising from its 2H and $1T'$ polymorphs have attracted intense interest.[1−3] The 2H-to-$1T'$ transformation is a semiconductor-to-metal transition and renders the normally inert basal plane of MoS_2 catalytically active toward H_2 absorption and evolution.[4,5] Thus, far, the research focus of the community is on exfoliated, 2D flakes of MoS_2 which are restacked into lamellar films for various applications.[6,7] Manish *et al.* show that restacked MoS_2 nanosheets enriched with the $1T'$ polymorph can achieve capacitance values up to 700 F cm^{-3} due to its high electrical conductivity.[8] Less attention has been directed at the crystal domain size and defect generation accompanying the 2H-to-$1T'$ phase conversion. Furthermore, the crystal structure of Li_xMoS_2 is not well understood despite two decades of study. The reason is that upon Li intercalation, the structure is dramatically modified and powder X-ray diffraction (XRD) often exhibits broad diffraction peaks, indicating a short structural coherence length.[9] Although electrochemical intercalation converts the $2H\text{-}MoS_2$ to a $1T'\text{-}Li_xMoS_2$ phase, the

electrochemical lithiation process is influenced by the charge uniformity of the sample, and lattice stress generated during the process results in inhomogeneous phase change.[10]

Herein, we show that the chemical intercalation of MoS_2 with lithium naphthalenide transforms it into a bulk nanostructured material (Li_xMoS_2), which can be viewed as a quasi-2D material with 2D layers separated by intercalants.[11] Our chemical intercalation method allows the Li concentration to be tuned such that the relative proportion of the 2H and $1T'$ phase can be controlled, producing nearly 100% $1T'$ phase at high Li intercalation. This allows us to correlate the performance of the resulting ternary composites in energy storage with the stoichiometry of the Li_xMoS_2 phase. As illustrated in Scheme 1, the 2H-to-$1T'$ phase conversion during chemical intercalation creates interleaved nanosized domains with three orientation variants; the nanocrystallinity engendered with the phase change allows a more homogeneous phase conversion and uniform charge distribution compared to the bulk MoS_2 as well as

Scheme 1. Schematic showing domain size reduction after chemical Li intercalation, which preempts the material to form nanocrystals during electrochemical Li intercalation.
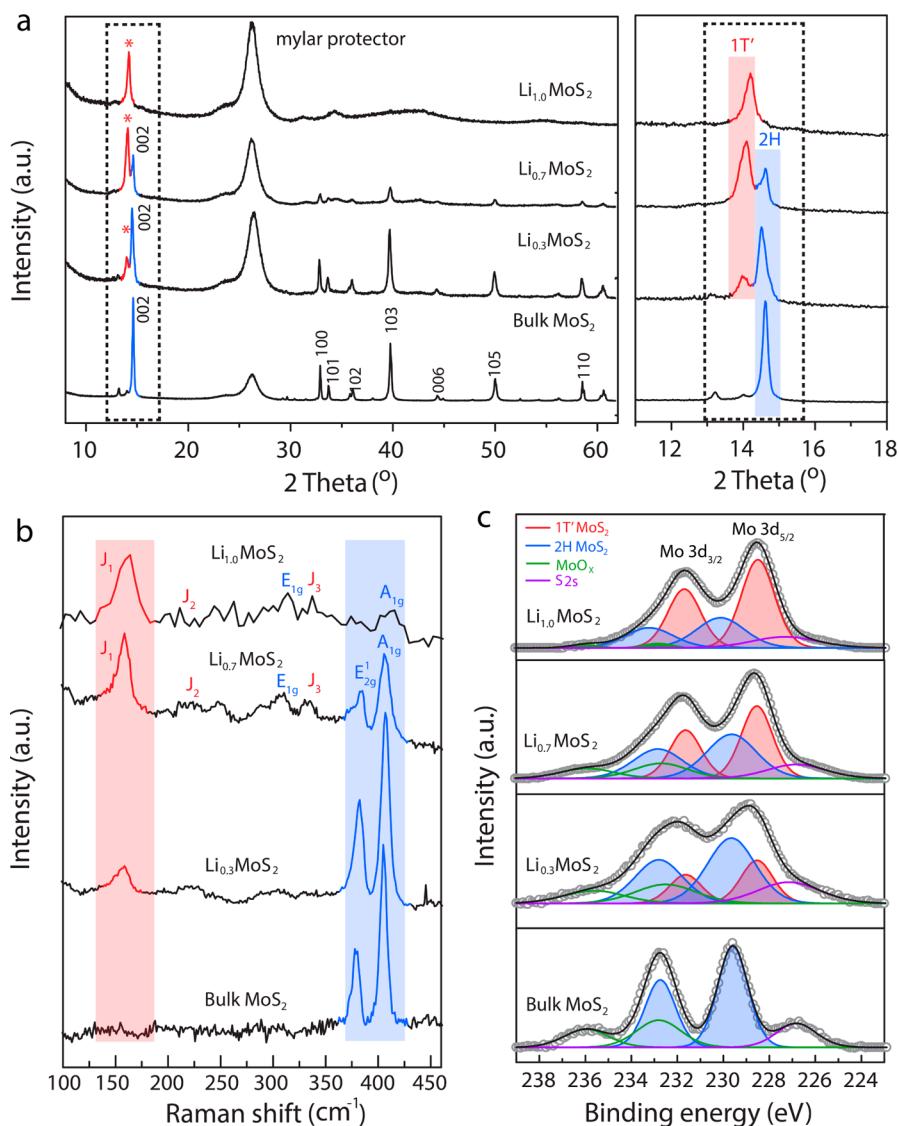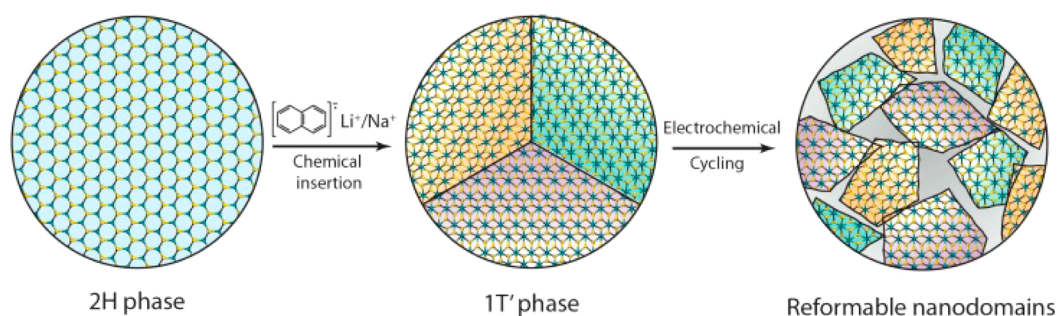
Figure 1. (a) Left: Wide scan XRD for bulk MoS_2 and also lithiated Li_xMoS_2 ($x \leq 1$). Right: Enlarged view spectra on the left, showing the evolution from 2H phase of bulk MoS_2 to the 1T′ phase of $Li_{1.0}MoS_2$. (b) Corresponding Raman spectra showing phase evolution from 2H to 1T′ as a function of Li concentration in Li_xMoS_2. (c) Corresponding XPS Mo 3d core level peak showing deconvoluted 2H and 1T′ components. Note that Mylar film and PMMA were used to protect the samples for XRD and Raman samples, respectively, but it could not be used in the case of XPS; thus the XPS samples had been exposed to air and some 1T′ phase had reverted to 2H.

restacked 2D MoS_2 sheets. Furthermore, these nanodomains introduced by chemical intercalation provide the preconditions for the formation of reformable nanocrystals in subsequent electrochemical phase conversion. As a result, these chemically intercalated TMDs demonstrate outstanding long-life cycling stability and rate capability in reversible lithium or sodium batteries; that is, 1T′-$Li_{1.0}MoS_2$ exhibits a capacity of 636 mA h g^{-1} at 1A g^{-1} for 2000 cycles.

RESULTS AND DISCUSSION

It is well known that the intercalation of Li in MoS_2 converts the semiconducting 2H MoS_2 to a metallic 1T/1T′ phase.[1,2,12−14] The transition to the 1T phase is caused by electron transfer from intercalated Li, which destabilizes the original trigonal-prismatic 2H-MoS_2 structure and favors octahedrally coordinated Mo atoms. The 1T phase then undergoes further distortion to form the 1T′ phase in order to lower the system energy. Figure 1a shows the phase evolution during the chemical intercalation using XRD, where it can be seen that the (002) peak of 2H-MoS_2 at 14.4° shifts by −0.2° to 14.2°, which is assigned to the (001) of Li-intercalated 1T′-MoS_2.[15] By controlling the relative concentrations of lithium naphthalenide to bulk MoS_2 powder during chemical intercalation, a mixed 2H/1T′ to fully converted 1T′ phase can be generated. Complementary Raman and XPS studies in Figure 1b and c support the XRD results, showing a Li-concentration-driven phase change from 2H to mixed 1T′ and finally to nearly full 1T′ phase. Figure 1b shows the Raman spectra of the phase-engineered sample at different Li:Mo compositions. 2H-MoS_2 can be clearly identified by the zone-center modes at 383 cm^{-1} (E_{2g}) and 409 cm^{-1} (A_{1g} modes). The 1T′ phase of MoS_2 is characterized by the disappearance of the E_{2g} peak and the appearance of new peaks at 158, 218, and 334 cm^{-1} corresponding to the J_1, J_2, and J_3 peaks, respectively.[16−18] These new peaks are associated with the reduced symmetry of the 1T′ phase.

Deconvoluted XPS spectra of the Mo 3d peak in Figure 1c allow the ratio of 1T′ and 2H phase to be followed as a function of Li concentration. The concentration of Li in the composite has been counter-checked using inductively coupled plasma elemental analysis. At increasingly higher amounts of inserted Li, chemically shifted components at 228.1 eV (Mo $3d_{5/2}$) and 231.4 eV (Mo $3d_{3/2}$), which are assignable to 1T′, increased in peak intensities relative to the 2H phase at 229.4 and 233 eV, respectively. Significantly, a 1T′-enriched phase (70%) can be achieved at high Li concentration (Li_xMoS_2 where $x > 1$), as evidenced by both Raman and XPS. However, along with the conversion to 1T′ phase, the overall crystallinity of the lithiated phase was observed to decrease dramatically, as judged by the reduced intensity and broadening of the (002) XRD peaks and the vanishing of the high-order diffraction peaks in Figure 1a.

Theoretical studies suggest that the 1T phase is dynamically unstable, and Peierls distortion reduces the dimensionality of this 2D system and breaks it into 1D zigzag chains, giving rise to the so-called distorted 1T phase (1T′).[19−21] The low-symmetry 1T′ phase has three orientation variants, resulting from the three equivalent directions of Peierls distortion in the parental 1T phase, which prevents the material from forming nanodomains during 2H-to-1T phase conversion.

To study the effect of 2H-to-1T′ phase conversion on the crystalline domains, we performed scanning transmission electron microscope (STEM) studies of the chemically lithiated flake. A typical bright field transmission electron microscopy (TEM) image of a lithiated MoS_2 flake is shown in Figure 2a. The corresponding selected area electron diffraction (SAED) pattern in Figure 2b clearly shows that our Li_xMoS_2 is dominated
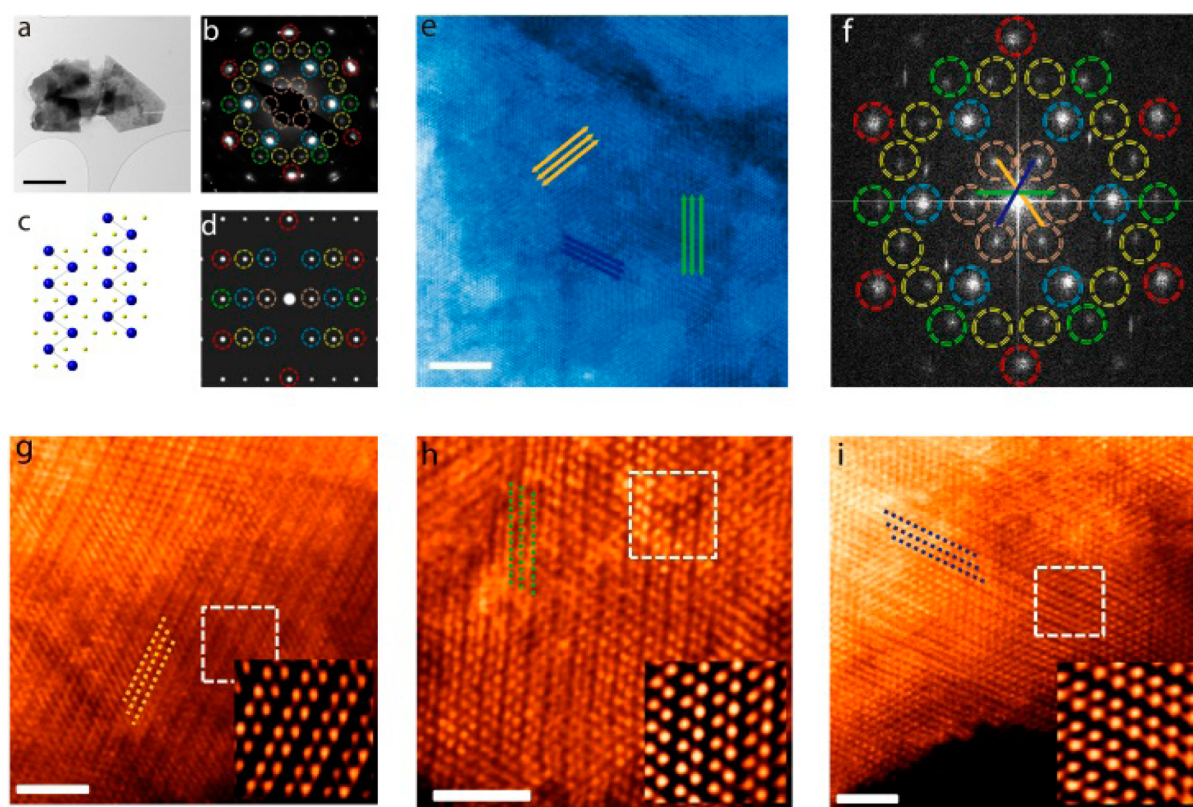
Figure 2. (a) TEM bright field image. (b) The corresponding SAED pattern of a typical bulk ternary Li_xMoS_2 flake. (c) Simulated model of (2 × 1) 1T′ structure. (d) SAED pattern along the (001) zone axis. (e) STEM-ADF image of 1T′ Li_xMoS_2 and (f) the corresponding fast Fourier transform (FFT) pattern with three orientation variants highlighted by yellow, blue, and green arrows. (g−i) STEM-ADF images of three typical grain orientations with inset showing filtered magnified images of three degenerate 1D zigzag chains. Scale bars: 500 nm in a; 5 nm in e; and 2 nm in g−i.

by a (2×1) 1T′ phase with the presence of the ~5.6 Å superstructure spots highlighted in orange and simultaneously with the missing of characteristic ~3.3 Å superstructure spots from the 1T″ phase as shown in Figure S1 and Table S1. The presence of three sets of superdiffraction spots further indicates that the sample contains multiple 1T′ domains with 1D zigzag chains along three primary directions. High-resolution STEM annular dark field (ADF) imaging in Figure 2e further confirms the presence of the 1T′ 2×1 superstructure spots with characteristic 1D zigzag chains along different orientations. Similar to the SAED results, the corresponding fast Fourier transform (FFT) pattern in Figure 2f of the STEM-ADF image shows a superposition of three sets of 1T′ diffractions along three degenerate directions, highlighted by the different color arrows. The spatial distribution of 1T′ domains can be obtained by Fourier filtering of the STEM-ADF imaging using each set of the 1T′ superdiffraction spots, as shown in Figure S2, and high-resolution STEM-ADF images of three domains are shown in Figure 2g−i, respectively. The STEM-ADF imaging results clearly show that the conversion of 2H into the 1T′ phase during chemical intercalation creates interleaved nanosized domains with different orientations, resulting in an overall maze-like structure.[22] Simultaneous with the 2H-1T′ phase transformation is a reduction in the grain size and the appearance of numerous domain boundaries and extended defects. The trend is generally toward a reduction in domain size of the material with increasing Li intercalation as shown in Figure S3.

Comparing bulk and chemically lithiated MoS$_2$, it can be seen that the interlayers of Li$_{1.0}$MoS$_2$ have expanded considerably compared to bulk MoS$_2$ (Figure 3a,b), giving a quasi-2D structure. Hydration and sonication of these lithiated samples results in the exfoliation of 2D flakes.[23] After subsequent washing and drying, a restacked film can be prepared, hereafter referred to as "restacked MoS$_2$" (Figure 3c). Due to the hydration treatment

used for expanding the layers, it is inevitable that some intercalated Li was removed during the washing step, which contributes to the loss of the 1T′ phase in the restacked MoS$_2$. XRD, Raman, and XPS verified that restacked MoS$_2$ films contain a mixture of 1T′ and 2H phases when freshly exfoliated, but most of the 1T′ phase converts back to the 2H phase upon exposure to air. XPS further demonstrates that the initial proportion of the 1T′ phase in freshly restacked MoS$_2$ is approximately 50%. In contrast, the unexfoliated Li$_x$MoS$_2$ presents a more stable and higher proportion of 1T′ phase, ~70% as judged from XPS and Raman studies in Figure 1. The 1T′ phase in Li$_x$MoS$_2$ can be maintained in the sandwiched layers.

The question may arise as to the necessity of chemical intercalation considering that when MoS$_2$ is used as electrode in lithium ion batteries, it will be subjected to electrochemical intercalation; thus a similar phase conversion process may ensue. Another issue is that such 1T′ phases, even if they are formed, are metastable. To answer the first question, we need to examine in detail the structural changes for a sample that has been subjected to chemical preintercalation (*e.g.*, Li$_{1.0}$MoS$_2$) and compare it with pristine, bulk MoS$_2$ subjected directly to electrochemical intercalation. Both samples were galvanostatically cycled under the same condition; then the samples were recovered from the battery coin cells at a delithiation stage and analyzed for their microstructural changes using STEM. The latter can perform element-specific imaging.

Figure 4a−c show structural evolution of the chemically intercalated 1T′ Li$_{1.0}$MoS$_2$ during discharge (lithiation). It is evident that the chemically lithiated material did not pulverize or crack after five galvanostatic cycles. The presence of interconnected nanocrystals of 3−4 nm size suggests the reforming of the MoS$_2$ nanocrystals during the phase conversion Li$_x$MoS$_2$ + $(4-x)$Li$^+$ + $(4-x)$e$^-$ ⇔ Mo + 2Li$_2$S. These nanocrystals persist even after 100 cycles of discharge/charge, as evidenced by STEM
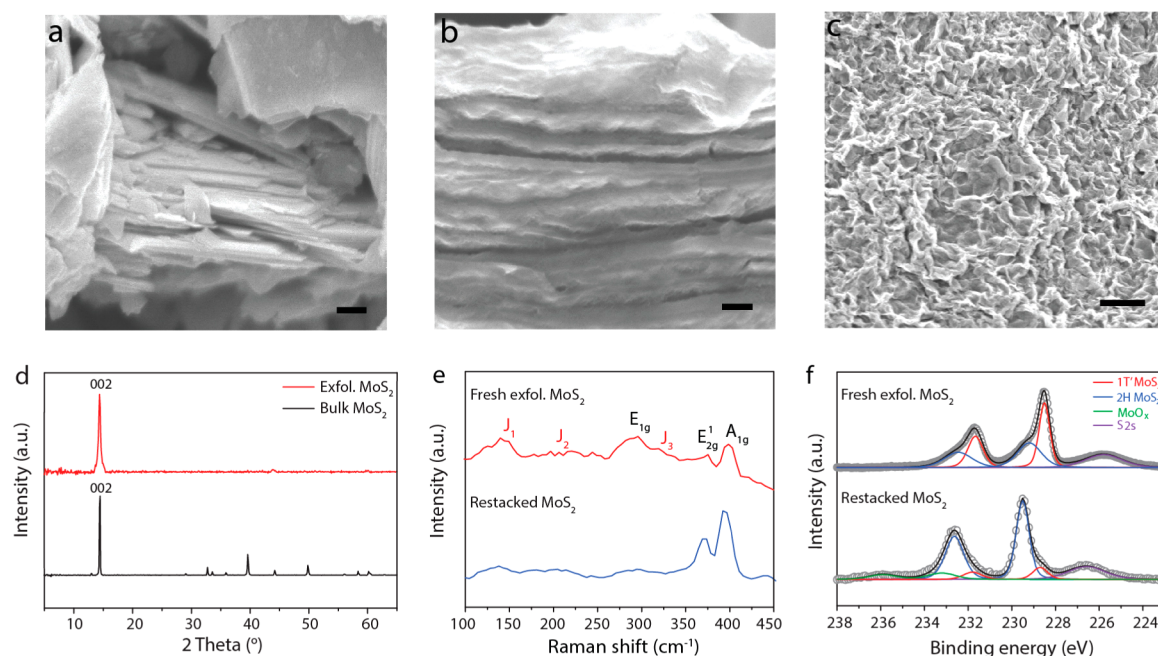
Figure 3. SEM images of bulk MoS$_2$, Li$_x$MoS$_2$, and exfoliated-restacked MoS$_2$. (a) Bulk MoS$_2$. (b) Li-intercalated Li$_x$MoS$_2$. (c) Restacked MoS$_2$. (d) XRD spectra of exfoliated and bulk MoS$_2$. (e) Raman spectra of freshly exfoliated MoS$_2$ showing 1T′ phonon modes and the reversal of the spectra to that which is characteristics of the 2H phase after air exposure and drying of restacked MoS$_2$. (f) XPS spectra showing 1T′-to-2H conversion following longer air exposure time. Scale bars: 100 nm in a and b and 2 μm in c.
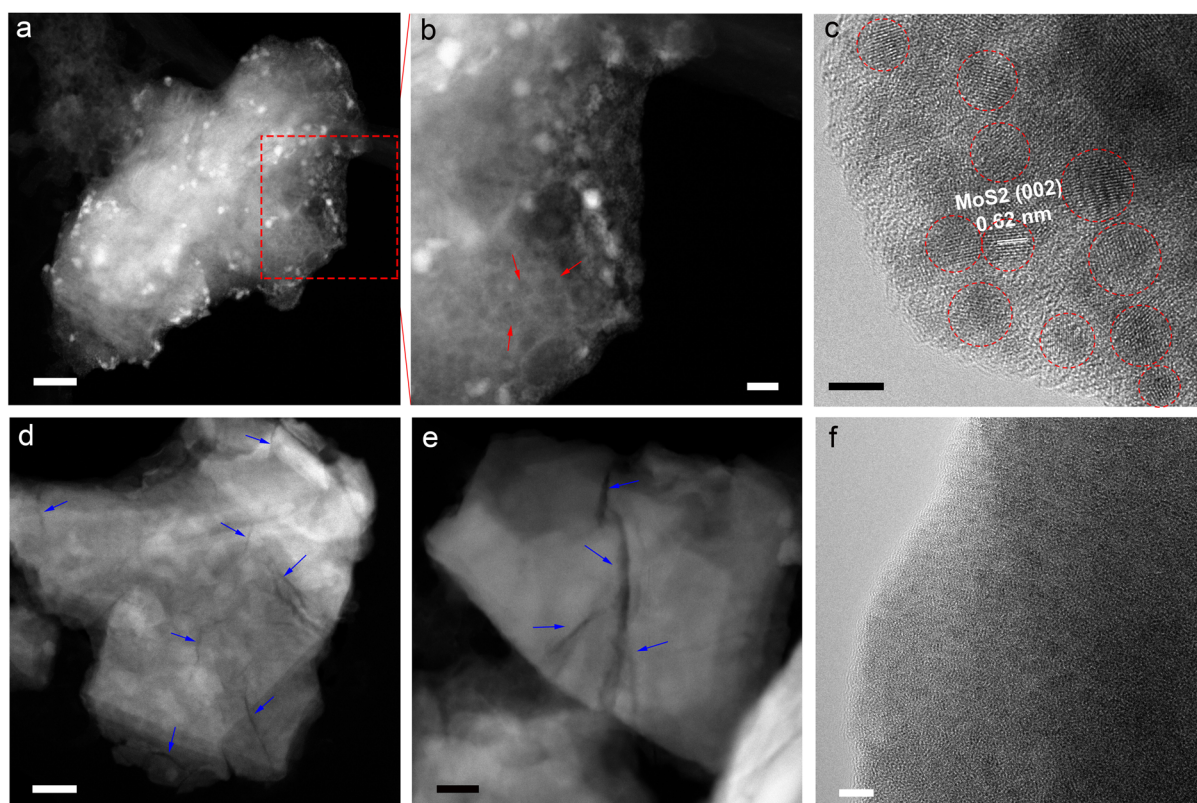
Figure 4. (a) STEM image of a $Li_{1.0}MoS_2$ electrode after 5 cycles and (b) the corresponding enlarged STEM image of sponge-like MoS_2 flake morphology, which is effective in accommodating volume expansion. (c) HR-TEM image of stable, reformable MoS_2 nanocrystals after 5 cycles in $Li_{1.0}MoS_2$. (d, e) STEM images of a bulk MoS_2 electrode after direct electrochemical intercalation of 5 cycles. It is obvious that cracks developed on the flake indicated by blue arrows after cycling. (f) HR-TEM image of a totally amorphous MoS_2 flake after 5 cycles. Scale bars are 200 nm in a and d; 50 nm in b; 100 nm in e, and 5 nm in c and f.

imaging in Figure S4. In these nanocrystals, Li^+ can be stored at higher dimensional defects, in particular at special interfacial cores between the nanocrystals and the amorphous matrix; for example, Li^+ can accumulate in the grain boundary cores, while electron clouds extend into neighboring crystalline areas.[24] In contrast, when bulk MoS_2 was directly electrochemically intercalated, it cracked and pulverized completely into an amorphous matrix after five cycles, as shown in Figure 4d–f.

The above studies show that it is important to create nanocrystallinity in the material prior to the galvanostatic cycling, as opposed to being created only at the cycling stage. Structural phase transitions that occur during battery lithiation, especially solid-state amorphization, are typically undesirable since they often lead to stress generation, slow kinetics, and poor cycle life. In that respect, the conversion of MoS_2 into a bulk nanocrystalline state, achieved by the chemical intercalation, bypasses multiple crystallographic transitions requiring high activation energies and allows the material to buffer the volume swings and phase conversion more efficiently. Although electrochemical intercalation also converts 2H to the 1T′ phase initially in the bulk MoS_2, this process is not as efficient because fluctuations in electrolyte exposure, electrical contact, or crystal defects give heterogeneous phase conversion.

To investigate if the nanostructuring of the crystal domains induced by chemical intercalation improves the subsequent battery performance, a systematic electrochemical study of bulk MoS_2, Li_xMoS_2, and exfoliated MoS_2 was carried out to compare the performance. Systematic studies of rate capability for bulk MoS_2 and preintercalated ternary $Li_{1.0}MoS_2$ are shown in Figure 5a.

It is clear that $Li_{1.0}MoS_2$ exhibits a faster and more stable charge/discharge rate compared to bulk MoS_2 and exfoliated MoS_2. The rate capability curves of Li_xMoS_2 (x from 0.3 to 1) ternary compounds are highly symmetrical, which demonstrate a highly uniform charge distribution (Figure S5).

In contrast, bulk MoS_2 batteries collapse rapidly even at a low current density of 1 A g^{-1}. Although exfoliated MoS_2 can charge and discharge from 0.1 A g^{-1} to 10 A g^{-1}, its rate capability curve shows hysteresis when cycling from low to high current and then back to low current, suggesting inhomogeneous charge distribution and capacity fading of the material. The cycling tests provide complementary evidence to the rate capability studies. The capacity of exfoliated MoS_2 decreases very quickly after 200 cycles at 1 A g^{-1} (Figure S6). $Li_{1.0}MoS_2$ exhibits a capacity of 636 mA h g^{-1} at 1 A g^{-1}, and ∼80% of the initial capacity is maintained even after 2000 cycles (Figure 5b). It must be pointed out that the capacity of $Li_{1.0}MoS_2$ can be boosted further by adding a higher amount of conductive carbon (40 wt %) to form a composite when making the electrode. For example a capacity of 1800 mAh g^{-1} can be obtained at 0.1 A g^{-1} when 40 wt % of carbon and super P is added (Figure S7). The stability test in Figure S8 shows that the performance scales with the proportion of Li preintercalated in the ternary phase material, for which the best performance is obtained with $Li_{1.0}MoS_2$. This is explained by the larger extent of domain size reduction with a higher degree of lithiation.

The greater charge uniformity in $Li_{1.0}MoS_2$ was confirmed using impedance spectroscopy. Figure 5c represents the typical Nyquist plot of an ion-insertion thin film electrode, where a
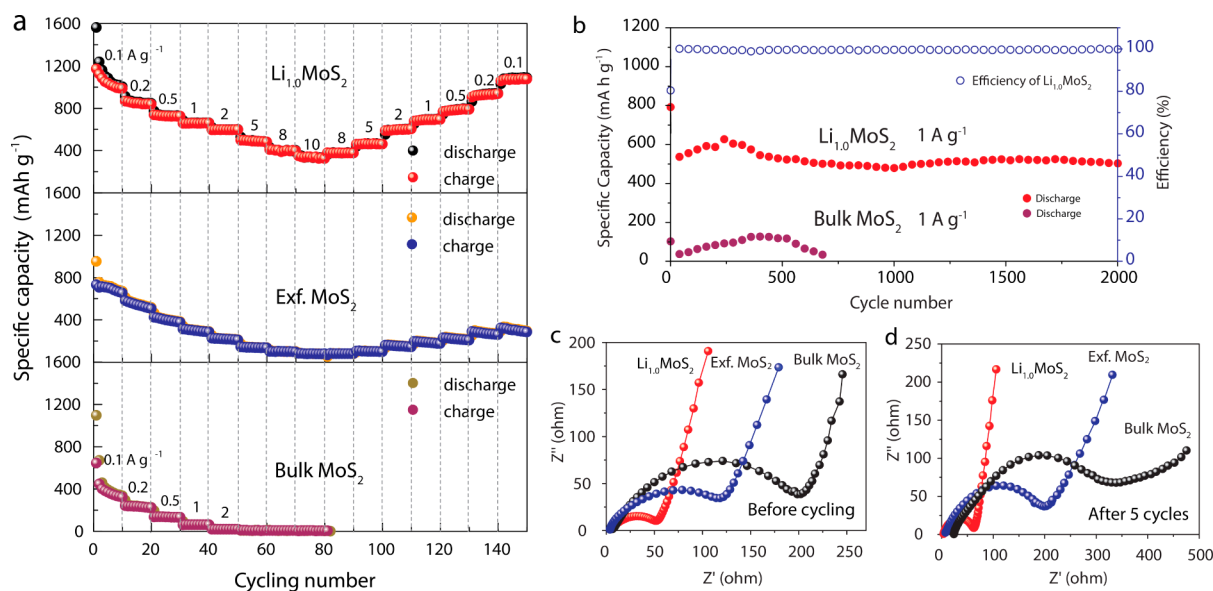
Figure 5. Electrochemical performance of Li$_x$MoS$_2$. (a) Nyquist plot of bulk MoS$_2$ and exfoliated MoS$_2$ and Li$_{1.0}$MoS$_2$ at the first and fifth cycles. (b) Rate capability plot for bulk MoS$_2$ and exfoliated MoS$_2$ and Li$_{1.0}$MoS$_2$. (c) Long-term cycle stability plot at 5 A g^{-1}. (d) Charge and discharge plots at different rates for bulk MoS$_2$ and Li$_{1.0}$MoS$_2$.
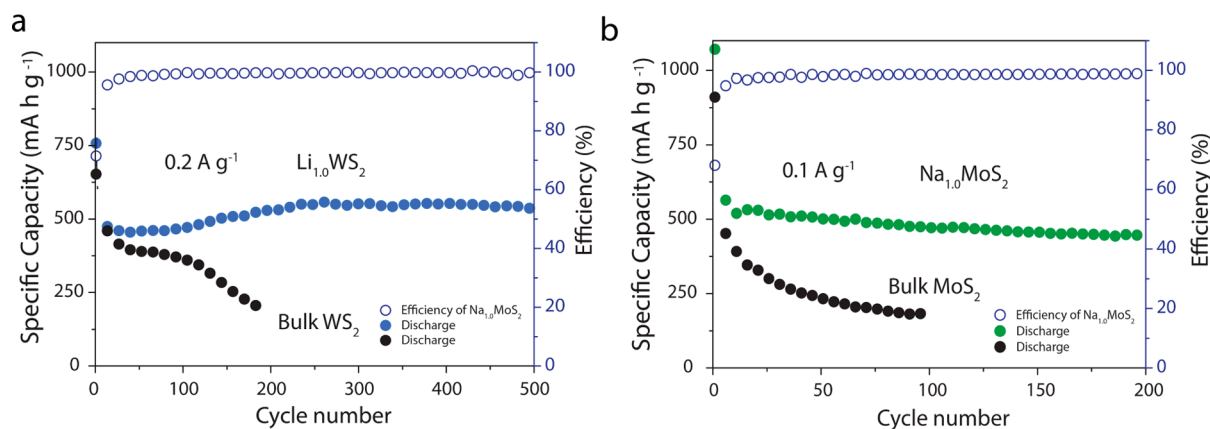
Figure 6. Cycle performance of (a) Li$_{1.0}$WS$_2$ and bulk WS$_2$ at 0.2 A g^{-1} for a Li-ion battery and (b) Na$_{1.0}$MoS$_2$ and bulk MoS$_2$ at 0.1 A g^{-1} for a Na-ion battery.

significantly smaller semicircle is observed for Li$_{1.0}$MoS$_2$ compared to exfoliated and bulk MoS$_2$ in the high-frequency region, and a steep sloping line exists at the lower frequency region due to the finite length effect. The significantly smaller semicircle is indicative of a correspondingly smaller charge transfer resistance (R_{ct} = 47 Ω cm^{-2}) in Li$_{1.0}$MoS$_2$ right from the first discharge cycle, which reflects the more uniform charge distribution and higher conductivity of 1T″-Li$_{1.0}$MoS$_2$. As shown in Figure 5d, the transfer resistance remains quite stable for Li$_{1.0}$MoS$_2$ at the fifth cycle (R_{ct} = 68 Ω cm^{-2}), whereas it increases in exfoliated and bulk MoS$_2$ to 199 and 323 Ω cm^{-2} (Table S2). A previous AFM conductivity mapping study has revealed the uniform metallic conduction in 1T′-MoS$_2$ and the inhomogeneous conductivity in the semiconducting 2H-MoS$_2$.[25] The more uniform metallic conduction avoids parasitic ohmic loss in 1T′-Li$_x$MoS$_2$ and allows electrical integration with the electrodes. In the case of exfoliated MoS$_2$, depending on the preparation conditions, a mixed phase 1T′/2H material is present, as opposed to the higher proportion and more uniform distribution of the 1T′ phase in Li$_x$MoS$_2$. Moreover, the disjointed boundaries in these restacked MoS$_2$ flakes give rise to a higher series

resistance compared to a bulk nanophase system such as 1T′-Li$_x$MoS$_2$, in which the electrical continuity of the layered scaffold remains relatively intact.

Most importantly, the generic applicability of the chemical intercalation on other bulk TMDs such as WS$_2$ has also been tested. In Figure 6a, we show that ternary phase Li$_{1.0}$WS$_2$ delivers improved cycling stability compared with bulk WS$_2$; a Li$_{1.0}$WS$_2$-based anode can be cycled for 500 cycles at 0.2 A g^{-1} without obvious capacity decay. Furthermore, chemical sodiation of MoS$_2$ using sodium naphthalenide has been carried out, in which Na$_{1.0}$MoS$_2$ demonstrates an impressive cycling capability of 500 mA h g^{-1} at 0.1 A g^{-1} for 200 cycles as shown in Figure 6b. Thus, chemical intercalation and phase engineering can be extended to other types of TMD host and alkali metal intercalants to make a bulk, alkali-metal intercalated nanophase material.

Along with the reduction in crystal domains size, both 2H and 1T′ XRD peaks decrease in intensity in XRD after the first cycle. However, the nanoscale structural change engendered in the 2H to 1T′ phase conversion is irreversible. The formation of such nanocrystalline domains generates interconnected domain boundaries and other extended 1D defects, which allows more

facile ion transport during electrochemical processes. Furthermore, due to the lower nucleation energy in these nanocrystalline states, it allows a more homogeneous phase conversion to Li_2S and *vice versa*, as can be seen from the presence of reformable MoS_2 nanocrystals after multiple galvanostatic cycles in STEM.

CONCLUSIONS

2H-to-1T′ phase conversion in bulk MoS_2 induced by chemical intercalation produces $Li_{1.0}MoS_2$, a bulk nanophase material. It exhibits a much higher cycle stability, capacity, and rate capability compared to pristine or exfoliated MoS_2 when used as an electrode material in lithium ion batteries. The elucidation of phase conversion in chemically intercalated MoS_2 using different characterization techniques allows us to correlate its electrochemical performance with the irreversible domain size reduction induced by chemical intercalation. Postcycling STEM analysis reveals that nanocrystalline grains in $Li_{1.0}MoS_2$ are reformable and robust, unlike samples that are directly electrochemically intercalated. Our work underscores the principle that chemical intercalation of bulk transition metal dichalcogenides may constitute a generic strategy of nanostructuring these materials for electrode application. Our work also suggests that as opposed to the tedious preparation of exfoliated and restacked 2D transition metal dichalcogenides, the nanostructuring of bulk MS_2 (where M = transition metal) compounds by chemical lithiation is an effective strategy for achieving high capacity and stable electrode material.

METHODS

1T′-$Li_{1.0}MoS_2$ Ternary Phase. All steps were operated in an argon-filled glovebox. A 0.48 g amount of naphthalene (Aldrich) and 20 mL of anhydrous tetrahydrofuran (THF) (Aldrich) were mixed thoroughly in a 40 mL capped bottle until naphthalene was fully dissolved. Then 0.052 g of Li (Aldrich) that had been cut into thin strips was added to the naphthalene—THF solution. After the addition of Li, the solution first became dark green and then changed to dark red. To guarantee that Li was completely dissolved, stirring was continued for another 40 min. After that, bulk MoS_2 powder (0.4 g; Aldrich) was added into the dark red solution and the mixture was further stirred for 2 h. The molar ratio of metal Li, naphthalene, and MoS_2 was 3:1.5:1. After reaction, the product was centrifuged five times at 3500 rpm using four 12 mL centrifuge tubes each time to remove impurities. Finally, the product was vacuum-dried.

$Li_{0.7}MoS_2$ Ternary Phase. A 0.034 g amount of Li, 0.48 g of naphthalene, and 20 mL of THF were mixed together, forming a dark green solution. At lower amounts of Li where $x < 1$ in Li_xMoS_2, the color of the solution was always dark green during 40 min of stirring. Then 0.4 g of bulk MoS_2 powder was added into the dark green solution, and the mixture was further stirred for 2 days. Here, the molar ratio of metal Li, naphthalene, and MoS_2 is 2:1.5:1. The following washing and drying steps were the same as the preparation process of $Li_{1.0}MoS_2$.

$Li_{0.3}MoS_2$ Ternary Phase. A 0.026 g amount of Li, 0.48 g of naphthalene, 0.4 g of bulk MoS_2, and 20 mL of THF were used, and the molar ratio of Li, naphthalene, and MoS_2 was 1.5:1.5:1. Then the mixture was further stirred for 2 days, and the rest of the preparation methods were similar to that of $Li_{0.7}MoS_2$. The preparation methods of $Li_{1.0}WS_2$ and $Na_{1.0}MoS_2$ are similar to that of $Li_{1.0}MoS_2$.

Exfoliated MoS_2 Nanosheet. Lithium naphthalenide was used for the exfoliation process.[23] In brief, 0.4 g of MoS_2 powder

was treated with 0.052 g of Li and 0.48 g of naphthalene for 1 day in a glovebox and exfoliated in cooled ultrapure water. The exfoliated MoS_2 was further dried in an oven prior to a battery test.

Characterizations. TEM was performed with a FEI Titan transmission electron microscope operated at 80 kV. STEM imaging and electron energy-loss spectroscopy (EELS) analysis were performed on an aberration-corrected Nion UltraSTEM-100 operating at 60 kV. XPS analysis was carried out on an Omicron EAC2000-125 analyzer. Al Kα radiation ($h\nu$ = 1486.6 eV) was employed as the X-ray source. Base pressure during analysis was 10^{-9} Torr. X-ray photoelectron spectra (Kratos AXIS UltraDLD XPS) were acquired using monochromatic Al Kα radiation ($h\nu$ = 1486.6 eV). Raman spectra were recorded at room temperature using a WITec Raman microscope with laser excitation at 532 nm.

Electrochemistry. The active material was first mixed with black carbon and a binder, poly(vinylidene fluoride), at weight ratio of 70:20:10. Then *n*-methylpyrrolidone was added into the mixture and stirred for 5 h to form a homogeneous slurry. The slurry was uniformly scraped on Cu foil with a blade, and subsequently the electrodes were vacuum-dried at 70 °C in the antechamber of the glovebox. After weighing, the active material loading in the electrode discs was about 3—4 mg cm^{-2}. CR2016-type coin cells were assembled in a glovebox for electrochemical characterization. A nonaqueous solution of 1 M $LiPF_6$ in a 1:1:1 (weight ratio) of ethylene carbonate, diethyl carbonate, and dimethyl carbonate was used as the electrolyte. Li metal discs were used as the counter electrodes for electrochemical testing. A Whatman glass microfiber filter was used as separator. Galvanostatic discharge—charge cycling of the batteries was monitored using a LAND battery tester. The cells were first galvanostatically charged and discharged in gradually increasing current densities from 0.1 A g^{-1} to 0.2, 0.5, 1, 2, 5, 8, and 10 A g^{-1} within the voltage range of 0.01—3 V at room temperature. All potentials hereafter are given *versus* Li/Li^+. Then the cells were charged and discharged back with the same decreasing current densities at the same voltage range. For the cycle stability test, the cell was first charged and discharged at 0.1 A g^{-1} for 10 cycles, then continued to cycle at 1 A g^{-1} for 2000 cycles. Cyclic voltammetry curves were collected by an Ivium-n-Stat multichannel electrochemical analyzer at 0.1 mV s^{-1} within a range of 0.01—3.0 V. Electrochemical impedance spectroscopy measurement was carried out on cells using an Autolab PGSTAT30 digital potentiostat/galvanostat at room temperature. The frequency was varied from 0.1 MHz to 10 mHz with an alternating voltage signal amplitude of 10 mV.

ASSOCIATED CONTENT

ⓈSupporting Information

The Supporting Information is available free of charge on the ACS Publications website at DOI: 10.1021/acsnano.6b05746.

Additional information (PDF)

AUTHOR INFORMATION

Corresponding Author

*E-mail (K. P. Loh): chmlohkp@nus.edu.sg.

Notes

The authors declare no competing financial interest.

ACKNOWLEDGMENTS

REFERENCES

(1) Chhowalla, M.; Shin, H. S.; Eda, G.; Li, L. J.; Loh, K. P.; Zhang, H. The Chemistry of Two-Dimensional Layered Transition Metal Dichalcogenide Nanosheets. *Nat. Chem.* **2013**, *5*, 263−275.

(2) Duerloo, K. A. N.; Li, Y.; Reed, E. J. Structural Phase Transitions in Two-Dimensional Mo- and W-Dichalcogenide Monolayers. *Nat. Commun.* **2014**, *5*, 4214.

(3) Voiry, D.; Mohite, A.; Chhowalla, M. Phase Engineering of Transition Metal Dichalcogenides. *Chem. Soc. Rev.* **2015**, *44*, 2702−2712.

(4) Chou, S. S.; Sai, N.; Lu, P.; Coker, E. N.; Liu, S.; Artyushkova, K.; Luk, T. S.; Kaehr, B.; Brinker, C. J. Understanding Catalysis in a Multiphasic Two-Dimensional Transition Metal Dichalcogenide. *Nat. Commun.* **2015**, *6*, 8311.

(5) Voiry, D.; Salehi, M.; Silva, R.; Fujita, T.; Chen, M.; Asefa, T.; Shenoy, V. B.; Eda, G.; Chhowalla, M. Conducting MoS_2 Nanosheets as Catalysts for Hydrogen Evolution Reaction. *Nano Lett.* **2013**, *13*, 6222−6227.

(6) Li, H.; Wu, J.; Yin, Z.; Zhang, H. Preparation and Applications of Mechanically Exfoliated Single-Layer and Multilayer MoS_2 and WSe_2 Nanosheets. *Acc. Chem. Res.* **2014**, *47*, 1067−1075.

(7) Lukowski, M. A.; Daniel, A. S.; Meng, F.; Forticaux, A.; Li, L.; Jin, S. Enhanced Hydrogen Evolution Catalysis from Chemically Exfoliated Metallic MoS_2 Nanosheets. *J. Am. Chem. Soc.* **2013**, *135*, 10274−10277.

(8) Acerce, M.; Voiry, D.; Chhowalla, M. Metallic 1T Phase MoS_2 Nanosheets as Supercapacitor Electrode Materials. *Nat. Nanotechnol.* **2015**, *10*, 313−318.

(9) Py, M. A.; Haering, R. R. Structural Destabilization Induced by Lithium Intercalation in MoS_2 and Related Compounds. *Can. J. Phys.* **1983**, *61*, 76−84.

(10) Wang, L.; Xu, Z.; Wang, W.; Wang; Bai, X. Atomic Mechanism of Dynamic Electrochemical Lithiation Processes of MoS_2 Nanosheet. *J. Am. Chem. Soc.* **2014**, *136*, 6693−6697.

(11) Luo, J.; Gao, J.; Wang, A.; Huang, J. Bulk Nanostructured Materials Based on Two-Dimensional Building Blocks: A Roadmap. *ACS Nano* **2015**, *9*, 9432−9436.

(12) Mattheiss, L. F. Band Structures of Transition-Metal-Dichalcogenide Layer Compounds. *Phys. Rev. B* **1973**, *8*, 3719−3740.

(13) Lin, Y. C.; Dumcenco, D. O.; Huang, Y. S.; Suenaga, K. Atomic Mechanism of The Semiconducting-to-Metallic Phase Transition in Single-Layered MoS_2. *Nat. Nanotechnol.* **2014**, *9*, 391−396.

(14) Eda, G.; Fujita, T.; Yamaguchi, H.; Voiry, D.; Chen, M.; Chhowalla, M. Coherent Atomic and Electronic Heterostructures of Single-Layer MoS_2. *ACS Nano* **2012**, *6*, 7311−7317.

(15) Tang, Q.; Jiang, D. E. Stabilization and Band-Gap Tuning of the 1T-MoS_2 Monolayer by Covalent Functionalization. *Chem. Mater.* **2015**, *27*, 3743−3748.

(16) Guo, Y.; Sun, D.; Ouyang, B.; Raja, A.; Song, J.; Heinz, T. F.; Brus, L. E. Probing the Dynamics of the Metallic-to-Semiconducting Structural Phase Transformation in MoS_2 Crystals. *Nano Lett.* **2015**, *15*, 5081−5088.

(17) Lee, C.; Yan, H.; Brus, L. E.; Heinz, T. F.; Hone, J.; Ryu, S. Anomalous Lattice Vibrations of Single- and Few-Layer MoS_2. *ACS Nano* **2010**, *4*, 2695−2700.

(18) Singh, A.; Shirodkar, S. N.; Waghmare, U. V. 1H and 1T Polymorphs, Structural Transitions and Anomalous Properties of $(Mo,W)(S,Se)_2$ Monolayers: First-Principles Analysis. *2D Mater.* **2015**, *2*, 035013−035016.

(19) Nasr Esfahani, D.; Leenaerts, O.; Sahin, H.; Partoens, B.; Peeters, F. M. Structural Transitions in Monolayer MoS_2 by Lithium Adsorption. *J. Phys. Chem. C* **2015**, *119*, 10602−10609.

(20) Li, W.; Li, J. Ferroelasticity and Domain Physics in Two-Dimensional Transition Metal Dichalcogenide Monolayers. *Nat. Commun.* **2016**, *7*, 10843−10846.

(21) Calandra, M. Chemically Exfoliated Single-Layer MoS_2: Stability, Lattice Dynamics, and Catalytic Adsorption from First Principles. *Phys. Rev. B: Condens. Matter Mater. Phys.* **2013**, *88*, 245428.

(22) Hu, T.; Li, R.; Dong, J. A New (2 × 1) Dimerized Structure of Monolayer 1T-Molybdenum Disulfide, Studied from First Principles Calculations. *J. Chem. Phys.* **2013**, *139*, 174702.

(23) Zheng, J.; Zhang, H.; Dong, S.; Liu, Y.; Chang, T. N.; Shin, H. S.; Loh, K. P. High Yield Exfoliation of 2-Dimensional Chalcogenides Using Sodium Naphthanelide. *Nat. Commun.* **2013**, *5*, 2995−2998.

(24) Maier, J. Thermodynamics of Electrochemical Lithium Storage. *Angew. Chem., Int. Ed.* **2013**, *52*, 4998−5026.

(25) Lukowski, M. A.; Daniel, A. S.; Meng, F.; Forticaux, A.; Li, L.; Jin, S. Enhanced Hydrogen Evolution Catalysis from Chemically Exfoliated Metallic MoS_2 Nanosheets. *J. Am. Chem. Soc.* **2013**, *135*, 10274−10277.